Front. Chem. Sci. Eng. 2021, 15(6): 1550–1560
https://doi.org/10.1007/s11705-021-2104-4

RESEARCH ARTICLE

Cobalt nanoparticle decorated N-doped carbons derived from a cobalt covalent organic framework for oxygen electrochemistry

Rui-Qi Zhang[1], Ang Ma[1], Xiang Liang[1], Li-Min Zhao[1], Hui Zhao (✉)[1], Zhong-Yong Yuan (✉)[2]

1 School of Materials Science and Engineering, Liaocheng University, Liaocheng 252000, China
2 Key Laboratory of Advanced Energy Materials Chemistry (Ministry of Education), School of Materials Science and Engineering, Nankai University, Tianjin 3000350, China

© Higher Education Press 2021

Abstract The low cost and highly efficient construction of electrocatalysts has attracted significant attention owing to the use of clean and sustainable energy technologies. In this work, cobalt nanoparticle decorated N-doped carbons (Co@NC) are synthesized by the pyrolysis of a cobalt covalent organic framework under an inert atmosphere. The Co@NC demonstrates improved electrocatalytic capabilities compared to N-doped carbon without the addition of Co nanoparticles, indicating the important role of cobalt. The well-dispersed active sites (Co–N_x) and the synergistic effect between the carbon matrix and Co nanoparticles greatly enhance the electrocatalytic activity for the oxygen reduction reaction. In addition, the Co content has a significant effect on the catalytic activity. The resulting Co@NC-0.86 exhibits a superb electrocatalytic activity for the oxygen reduction reaction in an alkaline electrolyte in terms of the onset potential (0.90 V), half-wave potential (0.80 V) and the limiting current density (4.84 $mA \cdot cm^{-2}$), and a high selectivity, as well as a strong methanol tolerance and superior durability, these results are comparable to those of the Pt/C catalyst. Furthermore, the superior bifunctional activity of Co@NC-0.86 was also confirmed in a home-built Zn-air battery, signifying the possibility for application in electrode materials and in current energy conversion and storage devices.

Keywords cobalt embedment, N-doped carbons, covalent organic framework, oxygen reduction, Zn-air battery

1 Introduction

Owing to the high energy conversion efficiency, environmentally friendly nature, good safety profile and the low volume of noise, proton exchange membrane fuel cells and rechargeable metal-air batteries are considered to be potential next-generation clean power sources [1]. The bottleneck preventing their practical implementation results from the sluggish kinetics of the oxygen reduction reaction (ORR) and the oxygen evolution reaction (OER) at the cathode, which involve a four-electron-transfer and multistep process. Pt-based noble metal catalysts are the type of electrocatalyst traditionally used for catalyzing the ORR, and RuO_2 and IrO_2 are usually the benchmark catalysts used in the OER [2,3]. However, the scarcity, high-cost and poor methanol resistance of noble metals limits their further development. Owing to this a tremendous amount of effort has been devoted to exploring non-noble metal electrocatalysts with low-costs, high efficiency and superior durability.

Transition metal nanoparticle-decorated N-doped carbon materials (TM-N/C) are regarded as promising candidates because they have been reported to exhibit abundant heteroatom dopants, a good porosity and a strong synergistic effect between the transition metal (TM) nanoparticles (TM-N) and the N-doped carbons [4–6]. However, uniform and high loading of TM-N on carbon materials is hard to achieve. In addition, the ORR catalytic performance is still inferior to that of the noble metal materials. Currently, the intrinsic nature of active sites has not been fully elucidated and this hinders further exploration of the TM-N/C catalysts [7,8]. Hence, suitable tuning of the porous structure and precise confinement of the active sites to achieve the controllable design of TM-N/C catalysts is of vital importance.

Received May 9, 2021; accepted July 30, 2021

E-mails: zhaohui@lcu.edu.cn (Zhao H),
zyyuan@nankai.edu.cn (Yuan Z-Y)

Covalent organic frameworks (COFs) are porous organic polymers constructed with various molecular secondary structural units via strong covalent bonds, which endow them with specific architectures, a high thermal stability and good chemical stability. Since they were first reported by Yaghi and coworkers in 2005, COFs have been used for various applications such as catalysis, separation and the detection of fluorescence [9–12]. The choice of structural unit in COFs is flexible, and this enables controllable construction of numerous accessible topological structures with different physicochemical properties. In addition, they often possess well-defined and predictable two dimensional (2D) or three dimensional (3D) crystalline structures resulting from the formation of covalent bonds through diverse synthetic organic reactions between the structural units, and therefore may allow precise control of the location of catalytic active sites [13]. The presence of N donor sites in COFs facilitates the strong grafting of metal ions and nanoparticles on the carbon matrix, leading to superior TM-N-carbon support interactions enabling fast electron transfer. Transition metals can be easily embedded into COFs by tuning the functionalities, enabling homogenous distribution and firm anchoring of the metal atoms [14–16]. Furthermore, the well-defined and tunable porosity of COFs is beneficial for confinement of the TM-N within the pore structures.

In this regard, COFs can act as an ideal platform to design advanced and highly efficient electrocatalysts, owing to their strong metal coordination capabilities, the abundance of nitrogen, the existence of C–N coordination sites and their good porosity. Several TM atoms such as Cu, Ni, Fe and Co have been introduced into COFs to form metal COFs (MCOFs) and further obtain TM-N/C catalysts through high-temperature pyrolysis under an inert atmosphere [17–20]. MCOFs combine the strengths of the controllable TM active sites and the structural framework of electrocatalysis, and can afford a large accessible surface area and rational electrocatalytic active sites enabling the desired activity and selectivity to be achieved. In addition, they can also provide a more critical understanding of the structure-activity relationships that exist in electrocatalysts. However, the electrocatalytic performance of MCOF-derived TM-N/C materials still requires improvement in order to compete with that of noble metals. Furthermore, it is critically important to explore COFs with further structural units in order to develop their intrinsic characteristics, achieving their controllable design and the precise confinement of active sites. Further investigations are required to understand the possible synergistic effect between the decorated metal nanoparticles and the COF-derived N-doped carbon matrix and to gain insights into the electrocatalytic mechanisms.

Herein, we prepared Co nanoparticle decorated N-doped carbons using a facile pyrolysis method of a hybrid of cobalt nitrate and a 2D COF, in which the COF was used as the nitrogen and carbon sources. The resultant Co@NC exhibits a superior catalytic activity, long-term stability and high methanol tolerance for the ORR, approaching that of the benchmark catalyst, Pt/C. When used as the air cathode in a home-built Zn-air battery (ZAB), a large peak power density and superior long-term durability were achieved, revealing significant potential for practical applications in ZABs. It was found that the remarkable electrocatalytic performance stems from the uniformly distributed Co nanoparticles, abundant N-doping, well-dispersed active sites ($Co–N_x$) and the synergistic effect between the carbon matrix and Co nanoparticles, as well as the high conductivities. The synthetic strategy developed in this work is believed to not only enrich the family of TM-N/C composites but could also inspire the controllable design of diverse structures from MCOFs.

2 Experimental

2.1 Synthesis of the TM-N/C catalysts

2.1.1 Synthesis of the COFs

1,3,5-Triformylphloroglucinol (TFP) (126 mg, 0.605 mmol) was first dissolved in a mixture of aniline (0.1 mL) and 1,4-dioxane (5 mL) and then heated at 40 °C in a water bath for 1 h. *p*-Phenylenediamine (PDA) (97.72 mg, 0.9 mmol) was dissolved in a mixture of 1,3,5-trimethylbenzene (5 mL) and acetic acid (36%, 5 mL). Subsequently, the above solution was transferred into an autoclave and heated to 120 °C for 72 h to obtain a dark red precipitate. The resulting precipitate was filtered, washed with tetrahydrofuran and extracted using a Soxhlet extractor for 24 h. The solid was dried in a vacuum at 80 °C to afford a dark red powder.

2.1.2 Synthesis of Co@NC

The COF powder (20 mg) was dispersed in acetonitrile (20 mL). Then, a certain amount of cobalt nitrate hexahydrate ($Co(NO_3)_2\cdot 6H_2O$) was added to the above solution with vigorous stirring at room temperature for 24 h. The cobalt ions-doped COF powder (Co-COF) was collected by centrifugation at 12000 $r\cdot min^{-1}$ for 10 min and dried overnight at 80 °C. Afterwards, the COFs were placed in a tube furnace and carbonized at 900 °C for 2 h with a heating rate of 5 $°C\cdot min^{-1}$ under a nitrogen atmosphere, they were then cooled naturally to room temperature to obtain the product, which was denoted as Co@NC. To investigate the influence of the Co contents, samples containing different contents of the Co element were synthesized under the same conditions except for the difference in the Co^{2+} concentrations (0.17, 0.86, and 1.53 $mmol\cdot L^{-1}$), denoted as Co@NC-*x* (x = 0.17, 0.86, 1.53). For comparison, the N-doped carbon sample

(denoted as NC) was also synthesized using a similar synthetic process without the addition of Co^{2+}.

2.2 Characterization

Scanning electron microscopy (SEM) was carried out on a Jeol JSF-7500L microscope at an acceleration voltage of 10 kV and transmission electron microscopy (TEM) was performed on a Jeol JEM-2100F microscope at 200 kV. Fourier transform infrared spectrometry (FTIR) spectra were recorded using a Nicolet iS50 instrument. Thermogravimetric analysis (TGA) was carried out using a Q600 (TA instruments, USA) from 25 °C to 800 °C at a heating rate of 10 °C·min^{-1} under an O_2 atmosphere. X-ray diffractometry (XRD) patterns was collected on a Rigaku SmartLab 9 diffractometer with Cu-Kα radiation (λ = 0.154 nm). N_2 sorption experiments were performed on a BELSORP-Max MicrotracBEL (Japan) isothermally at 77 K. The samples were all degassed at 473 K overnight prior to conducting the tests. The specific surface area was determined using the multipoint Brunanuer-Emmett-Teller (BET) method. On the basis of the adsorption branch of the isotherms and using the nonlocal density functional theory method, the pore size distribution curves were obtained. Raman spectra were collected on a Thermo-Fisher Scientific DXR spectrometer with a 532 nm radiation laser. X-ray photoelectron spectroscopy (XPS) was performed on a Kratos Axis Ultra DLD spectrometer with Al-Kα radiation (1486.6 eV).

2.3 Electrochemical tests

Working electrodes were prepared as follows. The catalyst (5 mg) was dispersed ultrasonically in 1 mL of 1:4 (v/v) Milli-Q water/isopropanol to obtain a homogenous dispersion. Nafion solution (0.5 wt-%, 20 μL) was then added into the above solution, then 10 μL of the dispersion was drop cast onto a polished 5 mm-diameter glassy carbon electrode. After drying at room temperature, the resulting electrode was used as the working electrode. The electrochemical measurements were performed using a Gamry Reference 3000 electrochemical workstation in an oxygen-purged 0.1 mol·L^{-1} KOH electrolyte. The reference electrode was Ag/AgCl, and the carbon rod was used as the counter electrode. For the ORR tests, the linear sweep voltammetry (LSV) and cyclic voltammetry (CV) curves were obtained at scanning rates of 5 and 20 mV·s^{-1} within a potential range from 1.2 to 0 V (*vs.* reversible hydrogen electrode (RHE)), respectively.

Rotating ring-disk electrode (RRDE) tests were carried out on a RRDE configuration with a glassy carbon disk and a Pt ring with an outer diameter of 7.92 mm and an internal diameter of 6.25 mm. The ring potential was set at 1.5 V (*vs.* RHE) to oxidize the HO_2^- intermediate. The peroxide percentage (%HO_2^-) and electron transfer number (n) were determined as follows:

$$x(H_2O_2) = \frac{2i_R/N}{i_D + i_R/N} \times 100\%,$$

$$n = \frac{4i_D}{i_D + i_R/N},$$

where i_D, i_R and N are the disk current, ring current and current collection efficiency (0.37), respectively.

For the OER tests, the LSV results were collected at a scan rate of 5 mV·s^{-1} and a rotating speed of 1600 r·min^{-1} within a potential range from 1.0 to 2.0 V (*vs.* RHE). Electrochemical impedance spectroscopy measurements were conducted at an overpotential mode from 0.01 to 100 kHz with an alternating current voltage of 5 mV.

A home-built liquid ZAB was assembled using a Zn plate as a cathode, 1 cm^2 of carbon paper loaded with 1 mg of the catalyst as an anode, and a 6.0 mol·L^{-1} KOH + 0.02 mol·L^{-1} $Zn(Ac)_2$ electrolyte. O_2 was fed to the catalyst by bubbling air over the cathode during the experiment. For comparison, the performance of the ZAB catalyzed by commercial Pt/C was used as a benchmark under identical settings.

3 Results and discussion

3.1 Materials synthesis and characterization

As shown in Scheme 1, the synthetic procedure for Co@NC basically involves three steps. $COF_{TFP\text{-}PDA}$ was

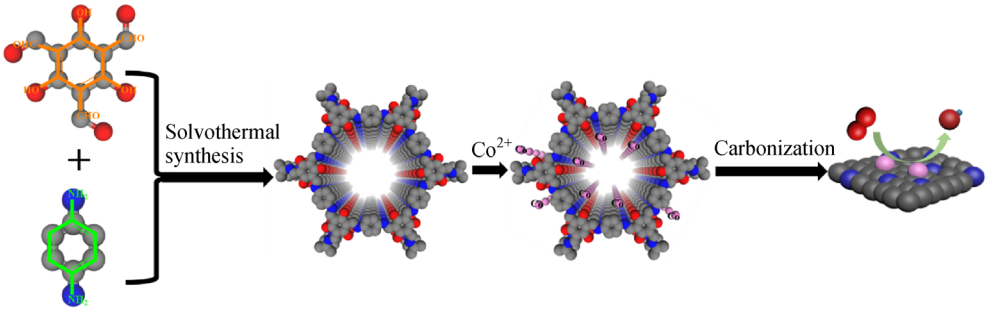

Scheme 1 Schematic procedure for the synthesis of Co@NC materials.

first synthesized based on a Schiff-base condensation between TFP and PDA under solvothermal conditions based on a previously reported literature method with a slight modification [21]. $COF_{TFP\text{-}PDA}$ was selected as the precursor for N-doped carbon owing to its 2D well-defined porous framework and unique heteroatom distribution that can facilitate mass transport and enhancement of the catalytic activity. Co^{2+} was then incorporated into $COF_{TFP\text{-}PDA}$ by coordination between Co^{2+} and N atoms in $COF_{TFP\text{-}PDA}$. The FTIR spectra for the COF and Co-COF-0.86 are shown in Fig. S1 (cf. Electronic Supplementary Material, ESM). The band at around 1257 cm^{-1} indicates the presence of a C–N group in the COF material. The shift of the C–N stretch for Co-COF-0.86, as compared with that of COF, results from Co–N coordination. After pyrolysis under an N_2 atmosphere, metal Co nanoparticles were stably anchored onto the COF-derived N-doped carbon materials.

The SEM and TEM images of the as-synthesized NC and Co@NC-0.86 are shown in Fig. 1. As shown in Fig. 1(a), the $COF_{TFP\text{-}PDA}$-derived NC sample displays a stacked rod-like structure. The cobalt nanoparticle decorated N-doped carbons (Co@NC) possess a similar plate-like morphology, in which a considerable number of Co nanoparticles are uniformly distributed on the N-doped carbon substrate (Fig. 1(b)). The corresponding element-mapping images of Co@NC-0.86 demonstrate that the Co, C, N and O elements are homogenously distributed within the material (Fig. S2, cf. ESM). The TEM image shown in Figs. 1(c) and 1(d) clearly reveals that the Co nanoparticles reside on the carbons and are homogenously distributed. The plate-like structure aggregated to form a macroporous structure, which could be beneficial to mass transfer during the ORR and OER process. Furthermore, the high-resolution TEM images (Figs. 1(e) and 1(f)) of the Co@NC exhibit distinct lattice fringes with a d-spacing of 0.205 nm, corresponding to the (111) facet of the cobalt nanoparticles. The average size of the cobalt nanoparticles is approximate 55 nm.

The XRD patterns of the $COF_{TFP\text{-}PDA}$ precursor (Fig. S3, cf. ESM) exhibit an intense peak at 4.7°, corresponding to the reflection from the (100) plane, and the minor peak at $2\theta = 26.5°$ corresponds to the reflection from the (001) plane, indicating the π–π stacking of the COF layers [21]. The COFs were converted to N-doped carbons after pyrolysis under an N_2 atmosphere. As shown in Fig. 2(a), the XRD pattern of NC exhibit two diffraction peaks at $2\theta = 25°$ and 44°, corresponding to the (002) and (100) planes of graphite, respectively [22]. Co@NC-0.17 presents a similar XRD pattern to that of the NC, this probably results from the addition of a relatively small amount of Co. The diffraction peaks for the Co@NC-0.86 and Co@NC-1.53 samples contain three typical peaks at $2\theta = 44.2°$, 51.6° and 76.1°, corresponding to the (111), (200) and (220) planes of metallic Co (PDF: 15-0806), respectively, these results are consistent with the SEM and TEM results. The broad diffraction profile demonstrates the low crystallinity. These results prove that the Co species were reduced to metallic Co nanoparticles during high-temperature pyrolysis. The Co content was evaluated using TGA, as shown in Fig. S4 (cf. ESM). The cobalt content was observed to be 2.83, 6.68% and 10.62 wt-% for Co@NC-0.17, Co@NC-0.86 and Co@NC-1.53, respectively.

Raman spectra were performed in order to examine the graphitization and the degree of defects present in the obtained samples. As observed in Fig. 2(b), all the materials show two prominent peaks situated at approximately 1346 and 1588 cm^{-1}, associated with the typical D and G bands, respectively, wherein the D band originates from the defective or disordered structure of the materials and the G band is attributed to the graphitic phases in the

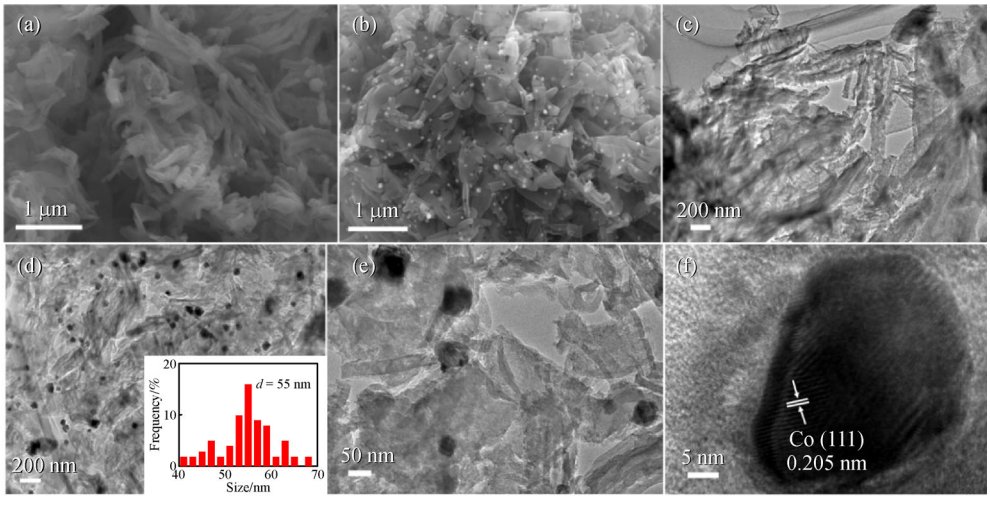

Fig. 1 SEM images of (a) NC, and (b) Co@NC-0.86; TEM images of (c) NC, (d, e) Co@NC-0.86, and high-resolution TEM image of (f) Co@NC-0.86.

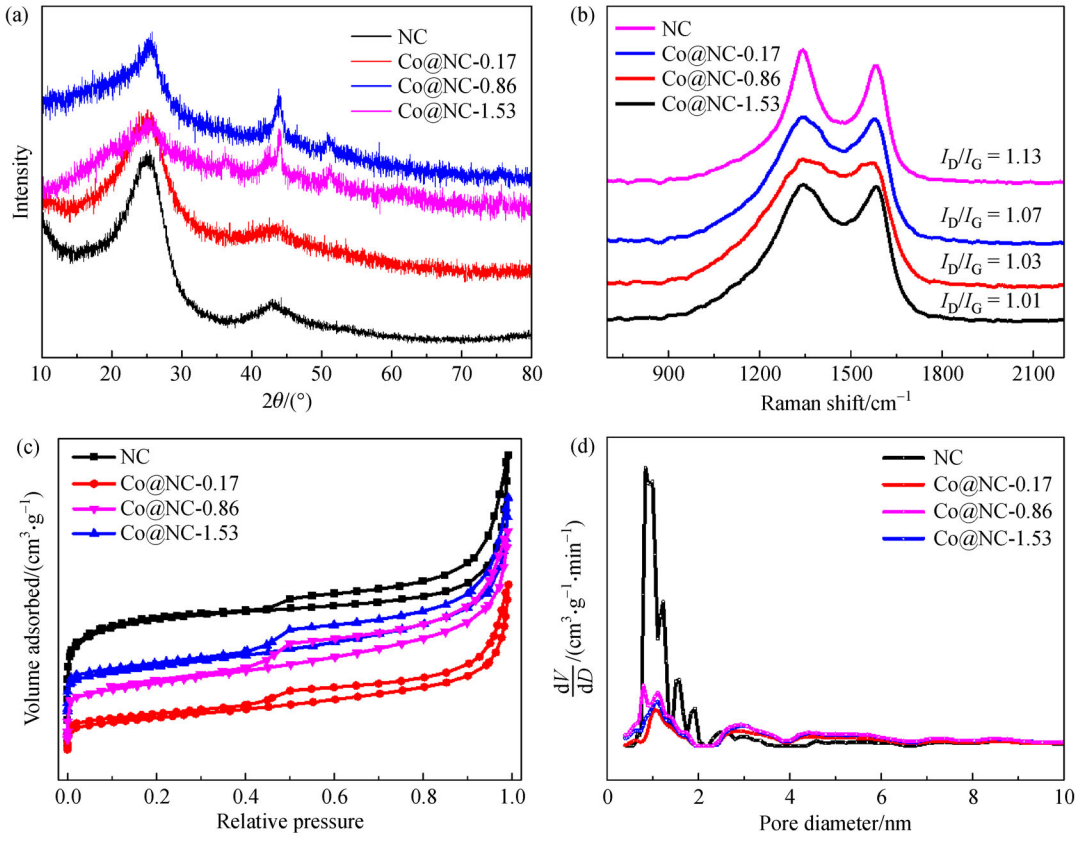

Fig. 2 (a) XRD patterns, (b) Raman spectra, (c) N_2 adsorption-desorption isotherm curves, and (d) pore size distributions of NC and Co@NC-*x*.

carbon [23]. The lower intensity ratio of the D and G band (I_D/I_G) of Co@NC, as compared with NC, indicates the higher degree of graphitization after decoration with the Co nanoparticle [24–26]. The I_D/I_G decreases from 1.07 to 1.01 for Co@NC-0.17 and Co@NC-1.53, respectively, which mainly results from the increasing degree of graphitization derived from the introduction of more Co nanoparticles. This can induce a high conductivity and facilitate enhancement of the electrocatalytic performance.

The porosity and textural characteristics of the synthesized samples were determined using N_2 adsorption-desorption analysis (Fig. 2(c)). All the samples show type II isotherms associated with type H3 hysteresis loops. The adsorption curves of the samples show a sharp rise at a low relative pressure, indicating the presence of abundant micropores. The existence of the mesopores is also indicated by the obvious hysteresis loop in the middle segment. Furthermore, the sharp rise in the adsorption curves at a high relative pressure corresponds to the aggregation of the plate-like structures, proving the presence of a large number of macropores. Table S1 (cf. ESM) lists the corresponding porous properties. It can be observed that the introduction of Co leads to a decrease in the BET specific surface area (407 $m^2 \cdot g^{-1}$ of NC and 51 $m^2 \cdot g^{-1}$ of Co@NC-0.17) and pore volume (0.787 $cm^3 \cdot g^{-1}$ of NC and 0.258 $cm^3 \cdot g^{-1}$ of Co@NC-0.17). However, the increase in the surface area and pore volume of Co@NC-*x* (182 $m^2 \cdot g^{-1}$, 0.367 $cm^3 \cdot g^{-1}$ of Co@NC-0.86 and 229 $m^2 \cdot g^{-1}$, 0.442 $cm^3 \cdot g^{-1}$ of Co@NC-1.53) was also observed after the introduction of further Co, probably because the presence of Co leads to the formation of abundant pores during pyrolysis. Hence, the relatively large pore volume and exposed surface area endow the catalyst with further active sites and enables facile contact with the reaction species, which is favorable for electrocatalytic reactions. As shown in Fig. 2(d) and Table S1, the pore diameter of the samples increases after introducing Co. Moreover, the pore size distribution curves prove the existence of both micropores and mesopores in the catalysts, which result from the condensation reaction of the COF precursors and the reaction between the Co species and carbon matrix during pyrolysis. The abundant porosity is conducive to accelerated mass transport during the electrocatalytic reaction.

To further investigate the chemical composition of the synthesized samples, XPS analysis was performed and the results are shown in Fig. 3 and in Figs. S5–S7. The peaks in the XPS survey spectra represent the presence of the elements Co, C, N and O in the Co@NC samples (Fig. 3(a)), while only the elements C, N and O can be

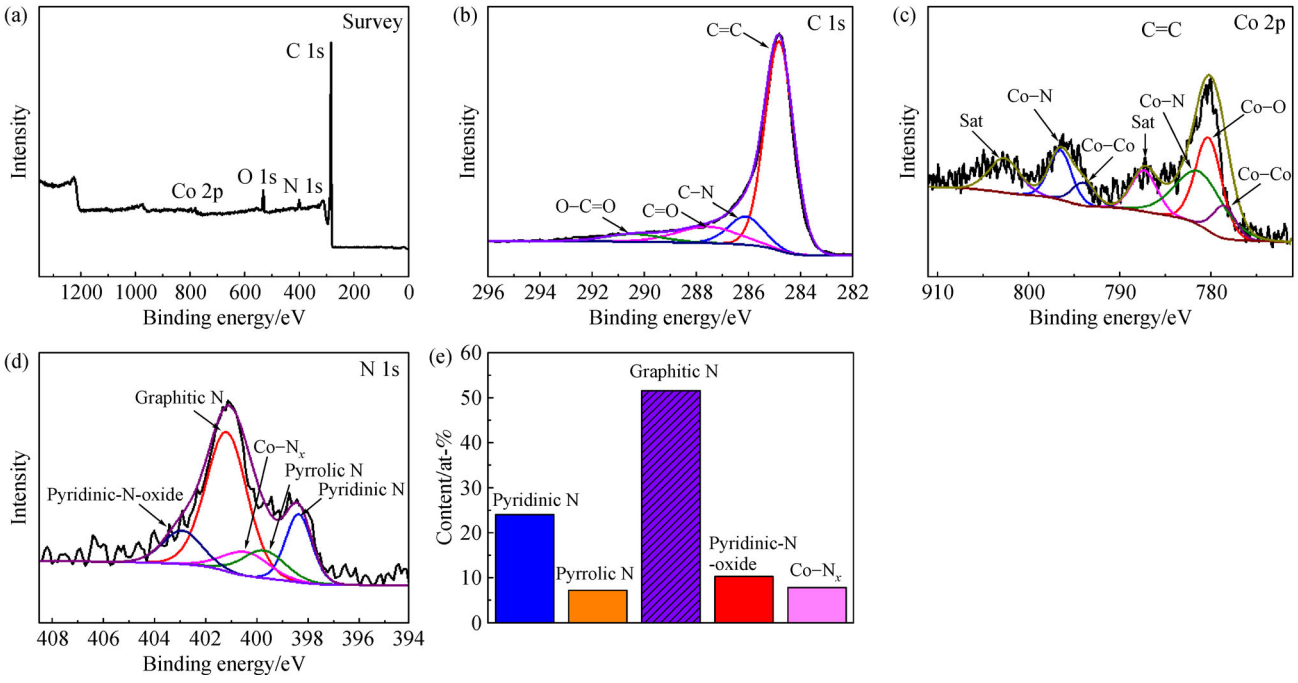

Fig. 3 (a) XPS spectrum of Co@NC-0.86; high-resolution spectra of (b) C, (c) Co, and (d) N; (e) percentages of pyridinic N, pyrrolic N, graphitic N, pyridinic-N-oxide, and Co–N_x in Co@NC-0.86.

observed in the NC sample (Fig. S5(a)). The peaks at 284.7, 285.6, 286.8 and 290.1 eV in the high-resolution C 1s spectrum correspond to C = C, C–N, C–O and O–C = O, respectively (Fig. 3(b)). The fitting of the Co 2p spectrum indicates the existence of Co–Co (778.5 and 793.6 eV), Co–O (780.2 eV) and Co–N (796.5 and 781.3 eV) with a couple of satellite peaks at 787.2 and 802.7 eV (Fig. 3(c)) [27,28]. Moreover, the deconvolution of the high-resolution N 1s spectrum of Co@NC-0.86 exhibits five peaks at 398.4, 399.5, 400.2, 401.0 and 403.1 eV (Fig. 3(d)), which can be attributed to the pyridinic N, pyrrolic N, Co–N_x, graphitic N, and pyridinic-N-oxide species, respectively [29–31]. The relative atomic percentages were calculated and found to be 24.17%, 7.26%, 10.31%, 51.55% and 7.71%, respectively (Fig. 3(e)). The graphitic N, pyridinic N and Co–N_x are the main species, these are well-known effective active sites for the ORR [32–34]. Among the three samples obtained by using different amounts of Co, Co@NC-0.86 was observed to possess the highest N atomic content of 6.19% compared with the other samples (Table S2, cf. ESM). In addition, Table S3 (cf. ESM) reveals that the Co–N_x content of Co@NC-0.86 is also higher than that of the other samples. The above analysis confirms that Co was incorporated into the carbon matrix in the form of metallic Co nanoparticles and Co–N_x sites, this is consistent with the results of the XRD analysis. Notably, the presence of a higher content of Co–N_x species can lead to a change in the electron cloud density of the adjacent carbon atoms, thus facilitating the adsorption/desorption capacities for the reaction species and further improving the electrocatalytic activity [35–37].

3.2 Electrocatalytic performance

To evaluate the electrocatalytic performance for the ORR, CV measurements of the catalysts and the commercial Pt/C catalyst were carried out using the rotating disk electrode technique in O_2-saturated 0.1 mol·L^{-1} KOH. All of the potentials were referenced to the RHE and the electrochemical data are shown in Fig. 4. As shown in Fig. 4(a), all the samples demonstrate a distinctive ORR peak. Among them, Co@NC-0.86 exhibits a quasi-rectangular-shaped CV curve with a higher characteristic ORR peak at approximately 0.81 V, close to that of the Pt/C benchmark (0.83 V), demonstrating the superior ORR activity. The LSV polarization curves of the synthesized Co@NC samples and Pt/C at a rotating speed of 1600 r·min^{-1} in O_2-saturated 0.1 mol·L^{-1} KOH are shown in Fig. 4(b). Without the addition of Co the NC catalyst exhibits an inferior electrocatalytic activity for the ORR with an onset potential of 0.75 V and a half-wave potential of 0.60 V, suggesting the significant importance of Co in enhancing the ORR performance. Among all the Co@NC catalysts, Co@NC-0.86 displays the best electrocatalytic properties with an onset potential of 0.90 V and a half-wave potential of 0.80 V. The limiting current density is also higher than that of the Co@NC-0.17 and Co@NC-1.53. The superior ORR performance of the Co@NC-0.86 is comparable to

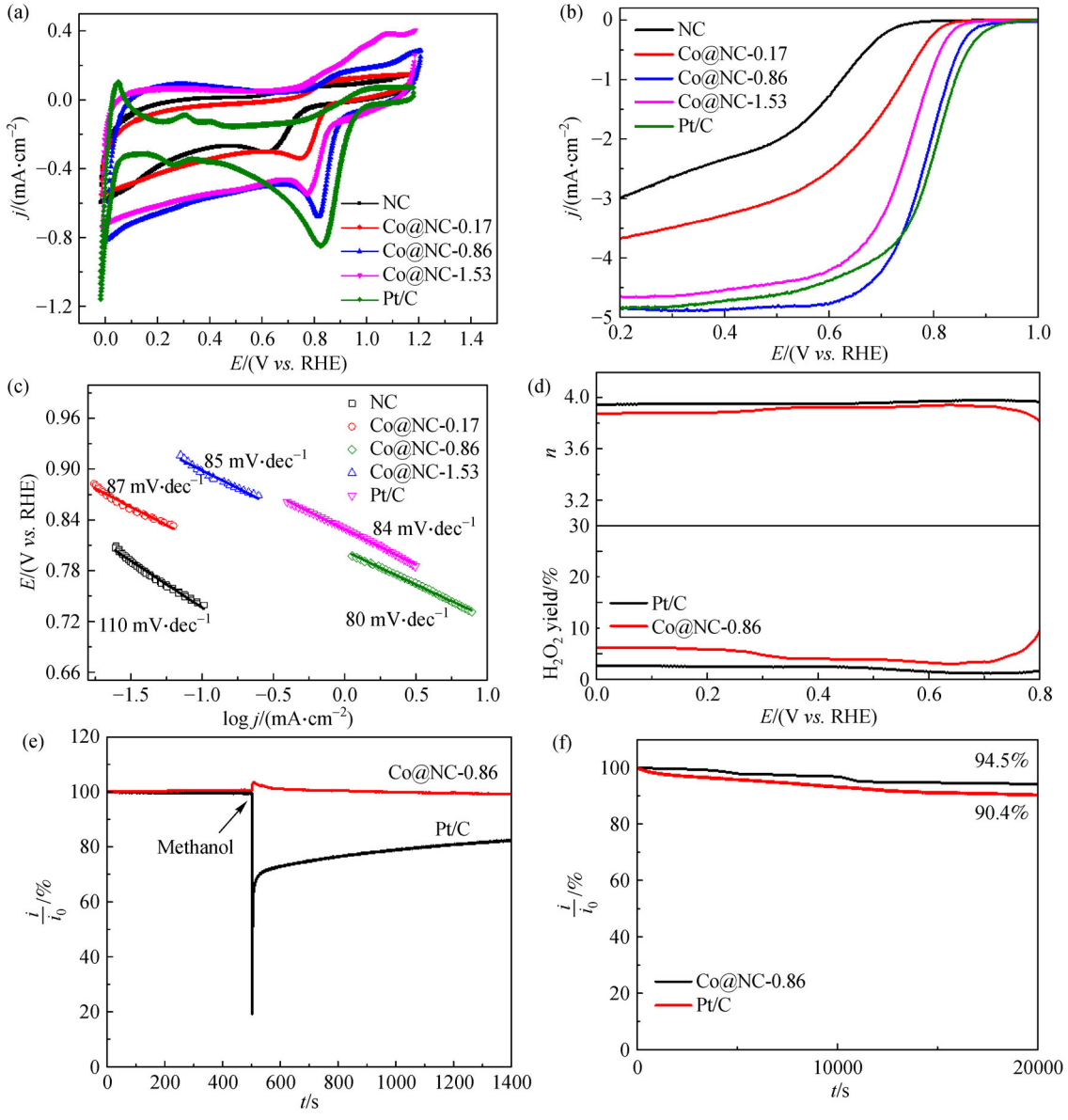

Fig. 4 (a) LSV and (b) CV curves of synthesized samples and Pt/C for ORR in O_2-saturated 0.1 mol·L^{-1} KOH; (c) ORR Tafel plots; (d) electron transfer number (n) and H_2O_2 yield of Co@NC-0.86 and Pt/C for ORR in O_2-saturated 0.1 mol·L^{-1} KOH; (e) i–t relation of resistance to methanol poison for Co@NC-0.86 and Pt/C through adding 5 mL 3 mol·L^{-1} methanol into solution; (f) chronoamperometric response of Co@NC-0.86 and Pt/C over 20000 s.

that of the benchmark catalyst, Pt/C, and is comparable to many other cobalt-based catalysts reported to date (Table S4, cf. ESM). The ORR performance decreases with the increase in the Co content, indicating that further Co content does not favor enhancement of the electrocatalytic performance. The results prove that a suitable Co content is indispensable to improving the ORR performance.

To further study the ORR catalytic kinetics, Tafel slopes for the catalysts are shown in Fig. 4(c). The obtained Tafel slope values were 110 and 87 mV·dec^{-1} for NC and Co@NC-0.17, respectively, demonstrating that the introduction of cobalt improves the ORR kinetics. Among the catalysts, the lower Tafel slope value obtained for Co@NC-0.86 (81 mV·dec^{-1}) in comparison to that of Pt/C (84 mV·dec^{-1}) further verifies its optimized ORR kinetics. This indicates that the first electron transfer reaction may be the rate-determining step of the ORR [38,39]. The limiting current densities gradually increase with elevated rotation speeds (Fig. S8, cf. ESM). A RRDE measurement with a ring potential of 1.3 V was also conducted to further investigate the reaction kinetics. As depicted in Fig. S9 (cf. ESM), Co@NC-0.86 exhibits a higher electron transfer number and lower H_2O_2 yield compared with that of the other samples. Figure 4(d)

reveals comparable kinetics between the Co@NC-0.86 and Pt/C with average values of n (3.91 *vs.* 3.97) and H_2O_2 yield (5.7 *vs.* 2.1) being obtained in the potential range of 0–0.8 V. This clearly indicates a $4e^-$-dominated transfer process for Co@NC-0.86 for the ORR. As shown in Fig. S10 (cf. ESM), the electrochemical double layer capacitance (C_{dl}) values of the materials were calculated from the CV test results in the non-Faradaic area, and were determined to be 0.77, 0.81, 1 and 1.65 $mF \cdot cm^{-2}$ for NC, Co@NC-0.17, Co@NC-0.86 and Co@NC-1.53, respectively. The specific capacitance can be converted into an electrochemical active surface area (ECSA) using the specific capacitance value for a flat standard with 1 cm^2 of real surface area (40 $\mu F \cdot cm^{-2}$). Thus, the ECSA values obtained were 19.25, 20.25, 25 and 41.25 cm^2, respectively. Moreover, in order to better understand the intrinsic activity, the turnover frequency (TOF) values at a potential of 0.6 V were also determined. The calculation process is shown in the ESM. The TOF value of Co@NC-0.86 is 0.00288 O_2 per s per site, this is higher than that of the Co@NC-0.17 (0.00156 O_2 per s per site) and Co@NC-1.53 (0.00252 O_2 per s per site), indicating a better catalytic activity. The mass activity values of the samples for the ORR at the potential of 0.6 V are 5, 10, 16.5 and 18.8 $A \cdot g^{-1}$.

In addition, the resistance of the catalysts to methanol poisoning was also investigated using chronoamperometry by adding 5 mL of 3 $mol \cdot L^{-1}$ methanol into 0.1 $mol \cdot L^{-1}$ KOH. It was observed that there was only a slight decline in the relative current for Co@NC-0.86, while a dramatic current decay was observed for Pt/C, as shown in Fig. 4(e). Hence, the superior tolerance to methanol crossover for the Co@NC-0.86 catalyst was proved. Furthermore, the long-term durability of high-efficiency ORR catalysts is essential during practical applications. A chronoamperometry test was carried out at a constant potential of 0.35 V (*vs.* RHE) in O_2-saturated 0.1 $mol \cdot L^{-1}$ KOH with a rotation rate of 1600 $r \cdot min^{-1}$. As observed in Fig. 4(f), Pt/C retained only 90% of its initial current. In contrast, Co@NC-0.86 exhibits 94.5% retention of the initial current over 20000 s during continuous operation, indicating a superb long-term durability for the ORR.

The OER performance of the as-synthesized samples was also evaluated in O_2-saturated 0.1 $mol \cdot L^{-1}$ KOH. As depicted in Fig. S11 (cf. ESM), after being decorated with Co nanoparticles, Co@NC displays enhanced OER activities compared with NC. Co@NC-0.86 affords the lowest overpotential of 590 mV to reach a current density of 10 $mA \cdot cm^{-2}$ compared with that of other Co@NC samples, which further proves the important effect of the Co content on the OER activity. Commercial Pt/C can afford an overpotential of 640 mV, reaching a current density of 10 $mA \cdot cm^{-2}$, which is higher than that of Co@NC-0.86, indicating that Co@NC-0.86 exhibits a high OER activity. As shown in the Nyquist plots (Fig. S12, cf. ESM), Co@NC-0.86 has a lower interface charge-transfer resistance as compared with NC, Co@NC-0.17 and Co@NC-1.53, revealing that the introduction of a suitable amount of Co endows the Co@NC-0.86 with a faster charge-transfer ability during the OER process. Furthermore, the overall oxygen electrode activity of the samples was investigated by examining the difference in the potential (ΔE) of the ORR (potential required at –3 $mA \cdot cm^{-2}$) and OER (potential required at 10 $mA \cdot cm^{-2}$). The small difference in the ΔE is required for practical applications. As observed in Fig. 5(a), Co@NC-0.86 presents the smallest value (0.93 V) among the synthesized Co@NC samples, indicating the superb bifunctional electrocatalytic performance.

To evaluate the practical catalytic performance of the Co@NC-0.86, a home-built ZAB with Co@NC-0.86 as the air cathode catalyst was fabricated (Figs. 5(b–f)). The ZAB delivers a high open-circuit voltage of 1.386 V (Fig. 5(b)), which is ascribed to the superior bifunctional electrocatalytic activity of Co@NC-0.86. The ZAB based on Co@NC-0.86 possessed a lower potential gap in the charge and discharge curves compared with the Pt/C catalyst based ZAB (Fig. 5(c)), indicating a good performance in practical devices. Based on the discharge curves, the power densities were calculated (Fig. 5(d)). Co@NC-0.86 can deliver a ZAB with a higher peak power density of 95 $mW \cdot cm^{-2}$ at a current density of 151.1 $mA \cdot cm^{-2}$ compared to that of the Pt/C (66 $mW \cdot cm^{-2}$ at 125.2 $mA \cdot cm^{-2}$). Furthermore, Co@NC-0.86 shows a stable charging voltage of 2.1 V and discharging voltage of about 1.2 V over 165 h and the Pt/C-based ZAB shows a significant performance decay over time (Fig. 5(e)), suggesting the superb cycling performance of Co@NC-0.86 in the cell configuration. As shown in Fig. 5(f), three Co@NC-0.86-based ZABs connected in series can light a white-light emitting diode, confirming their potential for use in practical applications. These results are comparable to recently reported ZABs assembled using transition metal-based catalysts (Table S5, cf. ESM).

According to previous reports, N-doping, in particular graphitic-N and pyridinic-N, is found to easily form defective complexes with carbon vacancies in the carbonaceous skeleton, modifying the charge distribution in the carbon ring and thereby serving as catalytic centers for the ORR and OER [40,41]. The NC sample without Co-decoration exhibits a higher N content and a higher percentage of pyridinic N and graphitic N species in comparison with Co@NC-0.17, however, it shows an inferior electrocatalytic performance. Hence, it is proposed that this difference in activity could be attributed to the presence of Co–N_x. Among the synthesized samples, the Co@NC-0.86 sample exhibits the highest content of Co–N_x and the highest catalytic activity for both the ORR and OER. It has been confirmed that the Co–N_x in carbon skeletons is mainly responsible for the superior performance of the Co@NC-0.86. The impressive catalytic properties of this catalyst are therefore ascribed to the

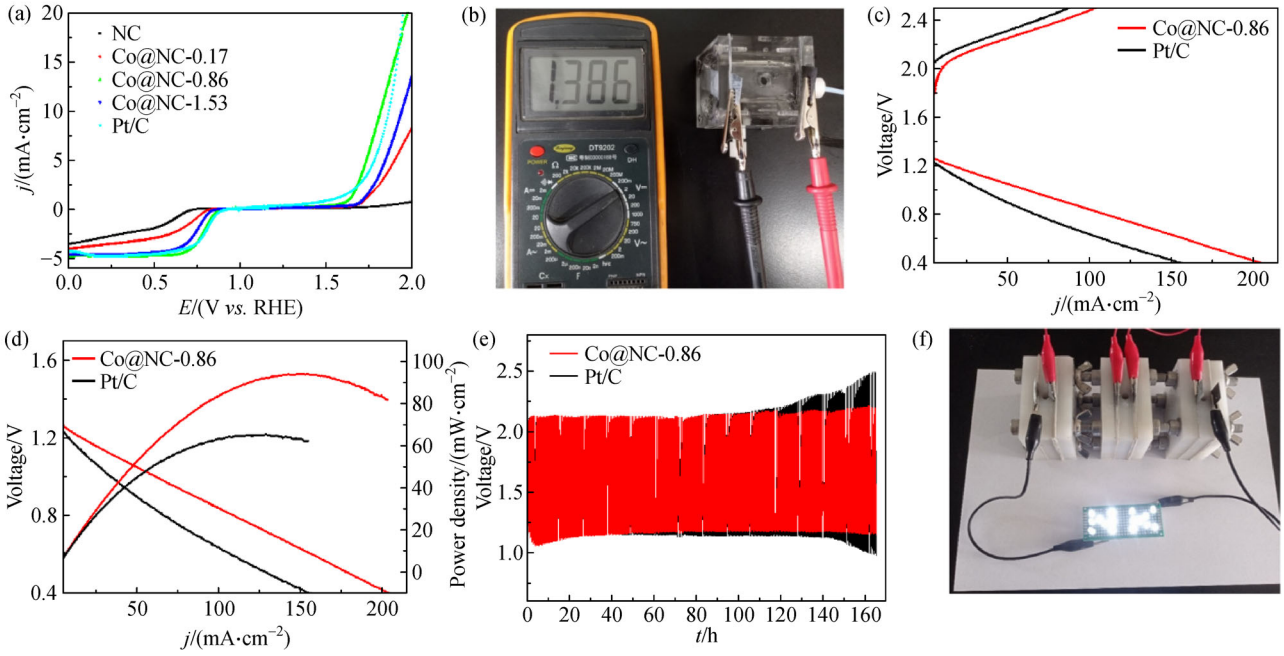

Fig. 5 (a) LSV curves of fabricated catalysts measured in the potential both ORR and OER; (b) optical photograph of the open-circuit voltage of the Co@NC-0.86 assembled ZAB; (c) the curves of Galvanodynamic charge/discharge polarization of the assembled ZAB; (d) the discharge polarization curves and the corresponding power densities of the assembled ZAB; (e) discharge-charge cycling curves of the Co@NC-0.86-assembled ZAB; (f) digital photograph of white-light emitting diode lit by the Co@NC-0.86-assembled ZABs (three) in series.

following features. 1) Uniformly distributed Co nanoparticle decorated N-doped carbons can be achieved by using a 2D well-defined COF as a precursor. The coordination interaction between the N and Co atoms results in the Co nanoparticles being firmly onto the carbon matrix and the formation of abundant Co–N_x sites. This can generate a synergistic effect between the Co nanoparticles and the N-doped carbon matrix, which significantly enhances the electrochemical performance. 2) The N-doping can alter the spin and charge densities of the adjacent carbon atoms, thus leading to an improved catalytic activity. The presence of Co nanoparticles increases the degree of graphitization, which can improve the electronic conductivity of the materials to facilitate electron transfer during the electrocatalytic reaction. 3) The Co content has a significant influence on the catalytic performance. Co@NC-0.17 possesses a reduced N content compared to that of NC. Among the as-synthesized samples, Co@NC-0.86 possesses the highest N atomic content, wherein the increased content of Co (Co@NC-1.53) leads to a decrease in the N content. Moreover, the decrease in the number of pyridinic N and Co–N_x active sites is also observed in Co@NC-1.53, further hampering the electrocatalytic performance. 4) The materials possess hierarchical micro-/meso-/macropore structures, which enable facile accommodation of further active sites, expediting mass transfer.

4 Conclusions

The cobalt nanoparticle decorated N-doped carbon (Co@NC) catalysts were obtained using a cobalt COF as a precursor. Electrochemical measurements show that the COF-derived catalysts possess a high ORR catalytic activity, selectivity, a superior tolerance to methanol crossover and long-term durability, which are comparable to those of the commercially available 20% Pt/C catalyst. The uniformly distributed Co nanoparticles, abundant N-doping, well-dispersed active sites (Co–N_x) and the synergistic effect between the carbon matrix and the Co nanoparticles, as well as high conductivities, contribute to an improvement in the ORR catalytic performance. In addition, the introduction of a suitable amount of Co has a significant effect on the ORR performance. The use of Co@NC-0.86 as an air catalyst in a home-built ZAB, results in a peak power density of 95 $mW \cdot cm^{-2}$ and a superior long-term durability, demonstrating its potential for practical applications. This work provides further insights into the development of synthetic methods for metal nanoparticle decorated carbon materials using N-containing COF as a precursor. The cobalt nanoparticle decorated N-doped carbons are also promising candidates for use as electrode materials in other energy conversion and storage fields, and will broaden the applications of COFs in carbon-based electrocatalysts.

Acknowledgements This work was supported by the Natural Science Foundation of Shandong Province (Grant No. ZR2019PB013), the Training Program of Innovation and Entrepreneurship for Undergraduates (Grant No. CXCY2021161), the Natural Science Foundation of Tianjin (Grant No. 19JCZDJC37700), and the National Natural Science Foundation of China (Grant No. 21875118).

Electronic Supplementary Material Supplementary material is available in the online version of this article at https://doi.org/10.1007/s11705-021-2104-4 and is accessible for authorized users.

References

1. Zhang H X, Liang J Y, Xia B W, Li Y, Du S F. Ionic liquid modified Pt/C electrocatalysts for cathode application in proton exchange membrane fuel cells. Frontiers of Chemical Science and Engineering, 2019, 13(4): 695–701
2. Peng X F, Wang Z H, Wang Z, Pan Y X. Multivalent manganese oxides with high electrocatalytic activity for oxygen reduction reaction. Frontiers of Chemical Science and Engineering, 2018, 12 (4): 790–797
3. Hao R, Ren J T, Lv X W, Li W, Liu Y P, Yuan Z Y. N-Doped porous carbon hollow microspheres encapsulated with iron-based nanocomposites as advanced bifunctional catalysts for rechargeable Zn-air battery. Journal of Energy Chemistry, 2020, 49: 14–21
4. Yin S H, Yang J, Han Y, Li G, Wan L Y, Chen Y H, Chen C, Qu X M, Jiang Y X, Sun S G. Construction of highly active metal-containing nanoparticles and $FeCo-N_4$ composite sites for the acidic oxygen reduction reaction. Angewandte Chemie International Edition, 2020, 59(49): 21976–21979
5. Ren J T, Yuan Z Y. A universal route to N-coordinated metals anchored on porous carbon nanosheets for highly efficient oxygen electrochemistry. Journal of Materials Chemistry A, 2019, 7(22): 13591–13601
6. Wu L M, Ni B X, Chen R, Sun P C, Chen T H. A general approach for hierarchically porous metal/N/C nanosphere electrocatalysts: nano-confined pyrolysis of *in situ*-formed amorphous metal-ligand complexes. Journal of Materials Chemistry A, 2020, 8(40): 21026–21035
7. Medard C, Lefevre M, Dodelet J, Jaouen F, Lindbergh G. Oxygen reduction by Fe-based catalysts in PEM fuel cell conditions: activity and selectivity of the catalysts obtained with two Fe precursors and various carbon supports. Electrochimica Acta, 2006, 51(16): 3202–3213
8. Wang H G, Weng C C, Yuan Z Y. Insights into efficient transition metal-nitrogen/carbon oxygen reduction electrocatalysts. Journal of Energy Chemistry, 2021, 56: 470–485
9. Zhao L M, Liu H M, Du Y, Liang X, Wang W J, Zhao H, Li W Z. An ionic liquid as a green solvent for high potency synthesis of 2D covalent organic frameworks. New Journal of Chemistry, 2020, 44 (36): 15410–15414
10. Liang X, Liu H M, Du Y, Li W Z, Wang M, Ge B, Zhao L M. Terbium functionalized covalent organic framework for selective and sensitive detection of LVX based on fluorescence enhancement. Colloids and Surfaces A, 2020, 606: 125429
11. Sharma R K, Yadav P, Yadav M, Gupta R, Rana P, Srivastava A, Zbořil R, Varma R S, Antonietti M, Gawande M B. Recent development of covalent organic frameworks (COFs): synthesis and catalytic (organic-electro-photo) applications. Materials Horizons, 2020, 7(2): 411–454
12. Rodríguez-San-Miguel D, Montoro C, Zamora F. Covalent organic framework nanosheets: preparation, properties and applications. Chemical Society Reviews, 2020, 49(8): 2291–2302
13. Li H, Chen F Q, Guan X Y, Li J L, Li C Y, Tang B, Valtchev V, Yan Y S, Qiu S L, Fang Q R. Three-dimensional triptycene-based covalent organic frameworks with ceq or acs topology. Journal of the American Chemical Society, 2021, 143(1): 2654–2659
14. Cui X, Lei S, Wang A C, Gao L K, Zhang Q, Yang Y K, Lin Z Q. Emerging covalent organic frameworks tailored materials for electrocatalysis. Nano Energy, 2020, 70: 104525
15. Yusran Y, Fang Q R, Valtchev V. Electroactive covalent organic frameworks: design, synthesis, and applications. Advanced Materials, 2020, 32(44): 2002038
16. Wang D, Qiu T, Guo W, Liang Z, Tabassum H, Xia D, Zou R. Covalent organic framework-based materials for energy applications. Energy & Environmental Science, 2021, 14(2): 688–728
17. Wang J, Wang J R, Qi S Y, Zhao M W. Stable multifunctional single-atom catalysts resulting from the synergistic effect of anchored transition-metal atoms and host covalent-organic frameworks. Journal of Physical Chemistry C, 2020, 124(32): 17675–17683
18. Wei S J, Wang Y, Chen W X, Li Z, Cheong W C, Zhang Q H, Gong Y, Gu L, Chen C, Wang D S, et al. Atomically dispersed Fe atoms anchored on COF-derived N-doped carbon nanospheres as efficient multi-functional catalysts. Chemical Science (Cambridge), 2020, 11 (3): 786–790
19. Roy S, Mari S, Sai M K, Sarma S C, Sarkar S, Peter S C. Highly efficient bifunctional oxygen reduction/evolution activity of a non-precious nanocomposite derived from a tetrazine-COF. Nanoscale, 2020, 12(44): 22718–22734
20. Zhu Y Z, Peng W C, Li Y, Zhang G L, Zhang F B, Fan X B. Modulating the electronic structure of single-atom catalysts on 2D nanomaterials for enhanced electrocatalytic performance. Small Methods, 2019, 3(9): 1800438
21. Kandambeth S, Mallick A, Lukose B, Mane M V, Heine T, Banerjee R. Construction of crystalline 2D covalent organic frameworks with remarkable chemical (acid/base) stability via a combined reversible and irreversible route. Journal of the American Chemical Society, 2012, 134(48): 19524–19527
22. Zhao H, Hu Z P, Zhu Y P, Ge L, Yuan Z Y. P-doped mesoporous carbons for high-efficiency electrocatalytic oxygen reduction. Chinese Journal of Catalysis, 2019, 40(9): 1366–1374
23. Zhao H, Weng C C, Ren J T, Ge L, Liu Y P, Yuan Z Y. Phosphonate-derived nitrogen-doped cobalt phosphate/carbon nanotube hybrids as highly active oxygen reduction reaction electrocatalysts. Chinese Journal of Catalysis, 2020, 41(2): 259–267
24. Yang Z, Zhao C, Qu Y, Zhou H, Zhou F, Wang J, Wu Y, Li Y. Trifunctional self-supporting cobalt-embedded carbon nanotube films for ORR, OER, and HER triggered by solid diffusion from bulk metal. Advanced Materials, 2019, 31(12): 1808043
25. Lv X W, Liu Y, Wang Y S, Liu X L, Yuan Z Y. Encapsulating vanadium nitride nanodots into N,S-codoped graphitized carbon for

synergistic electrocatalytic nitrogen reduction and aqueous Zn-N_2 battery. Applied Catalysis B: Environmental, 2021, 280: 119434

26. Weng C C, Ren J T, Hu Z P, Yuan Z Y. Nitrogen-doped defect-rich graphitic carbon nanorings with CoO_x nanoparticles as highly efficient electrocatalyst for oxygen electrochemistry. ACS Sustainable Chemistry & Engineering, 2018, 6(11): 15811–15821
27. Ouyang T, Ye Y Q, Wu C Y, Xiao K, Liu Z Q. Heterostructures comprised of Co/β-Mo_2C-encapsulated N-doped carbon nanotubes as bifunctional electrodes for water splitting. Angewandte Chemie International Edition, 2019, 58(15): 4923–4928
28. Aijaz A, Masa J, Rösler C, Xia W, Weide P, Botz A J R, Fischer R A, Schuhmann W, Muhler M. Co@Co_3O_4 encapsulated in carbon nanotube-grafted nitrogen-doped carbon polyhedra as an advanced bifunctional oxygen electrode. Angewandte Chemie International Edition, 2016, 55(12): 4087–4091
29. Wang Q, Zhou Z Y, Lai Y J, You Y, Liu J G, Wu X L, Terefe E, Chen C, Song L, Rauf M, et al. Phenylenediaminebased FeN_x/C catalyst with high activity for oxygen reduction in acid medium and its active-site probing. Journal of the American Chemical Society, 2014, 136(31): 10882–10885
30. Lefèvre M, Proietti E, Jaouen F, Dodelet J P. Iron-based catalysts with improved oxygen reduction activity in polymer electrolyte fuel cells. Science, 2009, 324(5923): 71–74
31. Lai L, Potts J R, Zhan D, Wang L, Poh C K, Tang C, Gong H, Shen Z, Lin J, Ruoff R S. Exploration of the active center structure of nitrogen-doped graphene-based catalysts for oxygen reduction reaction. Energy & Environmental Science, 2012, 5(7): 7936–7942
32. Guo D, Shibuya R, Akiba C, Saji S, Kondo T, Nakamura J. Active sites of nitrogen-doped carbon materials for oxygen reduction reaction clarified using model catalysts. Science, 2016, 351(6271): 361–365
33. Wu G, More K L, Johnston C M, Zelenay P. High performance electrocatalysts for oxygen reduction derived from polyaniline, iron, and cobalt. Science, 2011, 332(6028): 443–447
34. Cheon J Y, Kim J H, Kim J H, Goddeti K C, Park J Y, Joo S H. Intrinsic relationship between enhanced oxygen reduction reaction activity and nanoscale work function of doped carbons. Journal of the American Chemical Society, 2014, 136(25): 8875–8878
35. Zhang Y T, Wang P, Yang J, Lu S S, Li K K, Liu G Y, Duan Y F, Qiu J S. Decorating ZIF-67-derived cobalt–nitrogen doped carbon nanocapsules on 3D carbon frameworks for efficient oxygen reduction and oxygen evolution. Carbon, 2021, 177: 344–356
36. Sa Y J, Park S O, Jung G Y, Shin T J, Jeong H Y, Kwak S K, Joo S H. Heterogeneous Co–N/C electrocatalysts with controlled cobalt site densities for the hydrogen evolution reaction: structure-activity correlations and kinetic insights. ACS Catalysis, 2019, 9 (1): 83–97
37. Liu Y, Song C Y, Wang Y C, Cao W H, Lei Y P, Feng Q G, Chen Z, Liang S J, Xu L, Jiang L L. Rational designed Co@N-doped carbon catalyst for high-efficient H_2S selective oxidation by regulating electronic structures. Chemical Engineering Journal, 2020, 401: 126038
38. Tan Y, Xu C, Chen G, Fang X, Zheng N, Xie Q. Facile synthesis of manganese-oxide-containing mesoporous nitrogen-doped carbon for efficient oxygen reduction. Advanced Functional Materials, 2012, 22(21): 4584–4591
39. Liu S, Wang Z, Zhou S, Yu F, Yu M, Chiang C Y, Zhou W, Zhao J, Qiu J. Metal-organic-framework-derived hybrid carbon nanocages as a bifunctional electrocatalyst for oxygen reduction and evolution. Advanced Materials, 2017, 29(31): 1700874–1700883
40. Yang H B, Miao J W, Hung S F, Chen J Z, Tao H B, Wang X Z, Zhang L P, Chen R, Gao J J, Chen H M, et al. Identification of catalytic sites for oxygen reduction and oxygen evolution in N-doped graphene materials: development of highly efficient metal-free bifunctional electrocatalyst. Science Advances, 2016, 2(4): e1501122
41. Masa J, Xia W, Muhler M, Schuhmann W. On the role of metals in nitrogen-doped carbon electrocatalysts for oxygen reduction. Angewandte Chemie International Edition, 2015, 54(35): 10102–10120